Improving UAVSAR Results with GPS, Radiometry, and QUAKES Topographic Imager

**Andrea Donnellan, Yunling Lou, Curtis Padgett, Alan Tanner,
Brian Hawkins, Jay Parker, Adnan Ansar, Michael Heflin,
Joseph Green, Ronald Muellerschoen
Jet Propulsion Laboratory, California Institute of Technology
4800 Oak Grove Dr.
Pasadena, CA 91109
818-354-4737
andrea@jpl.caltech.edu**

Abstract— **UAVSAR is NASA's airborne interferometric synthetic aperture radar (InSAR) platform. The instrument has been used to detect deformation from earthquakes, volcanoes, oil pumping, landslides, water withdrawal, landfill compaction, and glaciers. It has been used to detect scars from wildfires and damage from debris flows. The instrument performs well for large changes or for local small changes. Determining subtle changes over large areas requires improved instrumentation and processing. We are working to improve the utility of UAVSAR by including GPS station position results in the processing chain, and adding a topographic imager to improve estimates of topography, 3D change, and damage. We are also exploring the benefit of microwave radiometry to mitigating error from water vapor path delay. A goal is to determine 3D tectonic deformation to millimeters per year at ~100 km plate boundary scales and to understand surface processes in areas of decorrelated radar imagery.**

TABLE OF CONTENTS

1. INTRODUCTION

Various methods are used to measure motions of the Earth's crust as a means of understanding geophysical processes such as earthquakes or volcanoes. Crustal deformation results from plate tectonics and earthquakes release elastic strain accumulation. Seismometers measure the waveforms generated by earthquakes. Aseismic deformation also occurs as a result of creep on faults and as strain accumulates and is released throughout the earthquake cycle. The method of measuring crustal deformation is referred to broadly as geodetic imaging. Measurement of crustal deformation adds information about rates and distribution of strain accumulation and release throughout the earthquake cycle. Understanding how strain is distributed along fault systems, how stress transfers through the crust along fault zones between earthquakes, and the fraction of aseismic versus seismic deformation, is key to assessing earthquake hazard for mitigating losses from future events [1].

Typically, crustal deformation measurements are made using precise Global Positioning System (GPS) stations or Interferometric Synthetic Aperture Radar (InSAR). GPS has the advantage of providing precise position time series at daily intervals or better. Accuracies are sub-mm globally and usually provide rates to better than 1 mm/yr. The disadvantage of GPS is that stations tend to be widely separated by 10 km or more making it difficult to infer smaller scale processes. InSAR on the other hand provides detailed images of deformation, but is collected less frequently and requires pairs of images to produce interferograms. A further limitation of InSAR is that the results provide line of sight measurements between the ground and the instrument at an oblique angle requiring multiple look angles to compute horizontal and vertical deformation. Water vapor path delay adds additional uncertainty to the results on the order of up to 5 cm. In this paper we explore methods to improve results produced by UAVSAR, NASA's Airborne InSAR platform.

2. UAVSAR

UAVSAR is NASA's L-band InSAR platform [2], which has been operational since 2009. It is flown on a Gulfstream-III aircraft. A precision autopilot enables repeated flights within a 10 m "tube" (typically ≤5 m) allowing sub-cm detection of surface deformation. UAVSAR has been used to measure surface motions from landslides [3], levees and subsidence [4], and earthquakes [5]. Flights have been operational in southern California since 2009 with flight paths repeated every few months to few years. Repeat pass interferometric (RPI) products are produced from these repeated flights.

978-1-5386-6854-2/19/$31.00 ©2019 IEEE

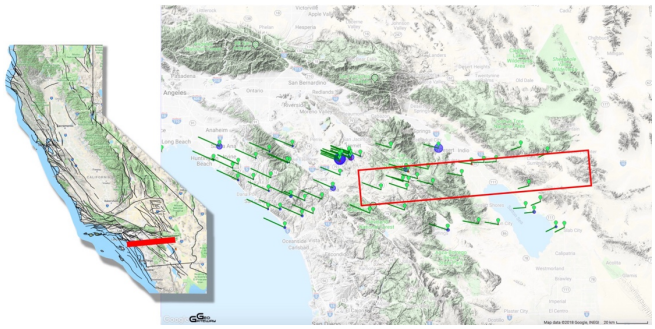

Figure 1. Location of UAVSAR line 26516 with nearby GPS stations and their long-term velocities. For the GPS adjustment displacements between the first and second pass are calculated.

An advantage of UAVSAR is its 7-meter pixel resolution, which is useful for measuring details of the spatial distribution of surface slip from faulting. Another advantage is its configurable flight path making it possible, for example, to select a look direction of the radar to be most sensitive to the direction of tectonic motion. UAVSAR can also be flown in response to events and was flown within a week of the M7.2 2017 El Mayor – Cucapah [5], M5.1 La Habra [6], and M6.0 South Napa earthquakes [7], where pre-earthquake measurements existed.

A limitation of InSAR in general is that the measurements decorrelate in areas of extensive surface disruption, which is common near ruptures of large earthquakes. Tropospheric water vapor delay and poor baseline estimation between repeat passes result in errors that limit the accuracy of determining surface deformation using UAVSAR. Comparing GPS measurements and motion estimates from UAVSAR pixels near the stations is a means of estimating errors in UAVSAR measurements. GPS position measurements are typically better than 1 mm globally [8], therefore making an excellent ancillary measurement for assessing the quality of UAVSAR and constraining the solutions. Tectonic-plate movement in many places may often be less than the day-to-day troposphere variation, however. Troposphere variation is a dominant error source that should be addressed concurrently.

3. Constraining Tectonic Motions

Airborne InSAR is challenging due to the irregular motion of the aircraft and limited ability to measure this motion. The UAVSAR InSAR calibration procedure uses geometric distortions of the imagery to estimate a correction to the motion measurements [9]. Very large geophysical changes, such as earthquakes or tectonic motions over long timescales, are a confounding signal to the motion calibration. We attempt to improve the calibration by accounting for surface deformation measured at GPS stations in the scene before estimating corrections to the radar motion (Figure 1). The concept is illustrated in Figure 2 where the UAVSAR scene contains 60 GPS stations. The three-dimensional point measurements are used to extrapolate the 3D displacement throughout the scene using a Kriging algorithm [10]. The

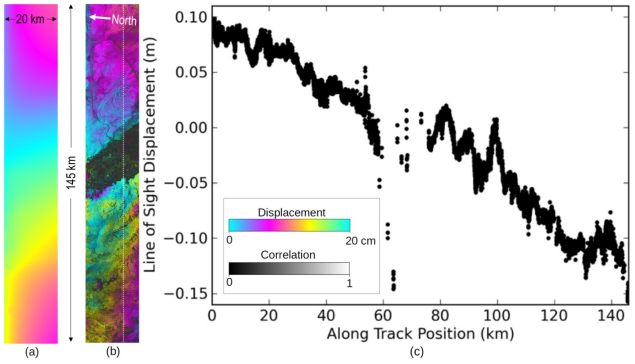

Figure 2. GPS-aided InSAR measurement. (a) Kriging of 60 GPS point measurements. The 3D displacements are projected into the radar line-of-sight and colored modulo 20 cm for comparison with the phase. (b) Unwrapped InSAR phase (colored modulo 20 cm) and correlation (gray scale). Swaths are 20x145 km. Heading in direction of top to bottom is 265°. (c) Profile of InSAR phase along dashed white line encompasses tectonic motion.

displacement field is projected onto the radar line-of-sight vector for each pixel in the scene to determine its contribution to the radar range measurements (Figure 2a). These contributions are subtracted from the range misregistration measurements that are used to refine the radar motion estimate. The GPS stations are too sparse to improve the solution in areas of high gradients, such as near earthquake ruptures, however, the measurements will improve the overall accuracy of motion across an entire scene for long wavelength motions.

One challenge presented by the long timespan is the tectonic motion occurring on large spatial and temporal scales. The standard UAVSAR interferometric processor assumes that image alignment artifacts are due to platform ephemeris errors and includes a procedure to estimate a correction from the image offset data in order to improve the interferometric correlation and phase measurements [11]. When the scene includes actual displacements on the order of the phase measurement of a few cm at spatial scales commensurate with the synthetic aperture length of a few km, then the assumption of the ephemeris correction procedure becomes invalid. That is clearly the case here where tectonic motion of several cm per year has accumulated.

In order to prevent the tectonic motion from being absorbed by the ephemeris correction, we used GeoGateway to query data from 60 GPS stations located near the study site. The 3D GPS displacements that occurred between the two SAR acquisitions were used as inputs to a kriging algorithm that generated 3D displacements at all points in the radar scene. The displacements were projected into the radar line of sight and cross-range directions. The LOS component is shown in Figure 2c. These components were subtracted from the image registration offsets prior to the ephemeris correction procedure. The line of sight change across the line of 220 mm over a 7.5 year timespan of the image pair yields a line of sight change of 33 mm/yr. Assuming an approximate

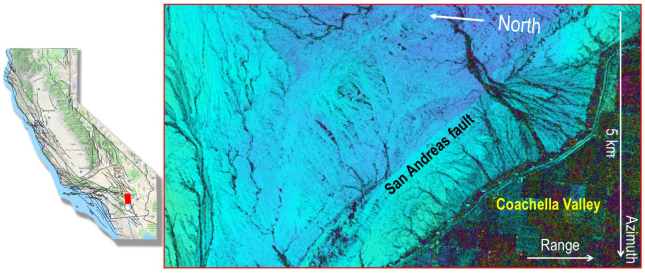

Figure 3. San Andreas fault near the Coachella Valley. The sharp color contrast across the fault is indicative of slip on the fault.

elevation angle between the ground and the instrument on aircraft of 45° yields a horizontal rate of 47 mm/yr, which is consistent with the Pacific – North American plate rate of 52 mm/yr [12], particularly since the processed line does not cover the entire width of the plate boundary zone.

Another challenge with this scene concerns the temporal decorrelation of the agricultural areas in the Coachella valley. The valley spans the entire range swath, effectively splitting the image into two disparate pieces. This presents a severe problem for both the ephemeris correction and phase unwrapping procedures, since each algorithm essentially has to integrate across the image. For the ephemeris correction, the two segments were processed separately, and the two solutions were merged via a spline fit. The phase was unwrapped using the SNAPHU algorithm [9], which in this case was better able to integrate across the decorrelated region than the usual UAVSAR phase unwrapper [10]. The final result is shown in Figure 2b which demonstrates good agreement with the GPS data.

This method produces an interferogram, that matches the long-term tectonic motion (Figure 2c) and produces a clean image locally (Figure 3). The interferogram, spans 7.5 years and includes the 2010 M7.2 El Mayor-Cucapah earthquake, which ruptured Baja California, Mexico up to the US Mexican border about 115 km to the south of the line [13]. The event triggered slip on the San Andreas fault. This triggered slip is clearly seen in a zoomed in image of the processed line adjusted with GPS motions (Figure 3). Further analysis will enable determination of how much slip was triggered by the earthquake and whether slip continued following the event.

3. TROPOSPHERIC ERROR

Tropospheric variations can be estimated using GPS (figure 4) over a relatively small area of about 20 x 20 km. Troposphere solutions among four sites in the Mojave Desert in California, USA varies as much as 5 cm, and there appears to be a west to east drift (relative to GPS station RSTP) of around 2400 seconds for GPS station PHLB and 3300 seconds for GPS station HIVI. The Rosamond Corner Reflector Array (RCRA) is used, in part, to calibrate electronic radar delays in the UAVSAR instrument. These electronic delays are correlated with the troposphere. Recent calibrations have backed off on adjusting the electronic delay,

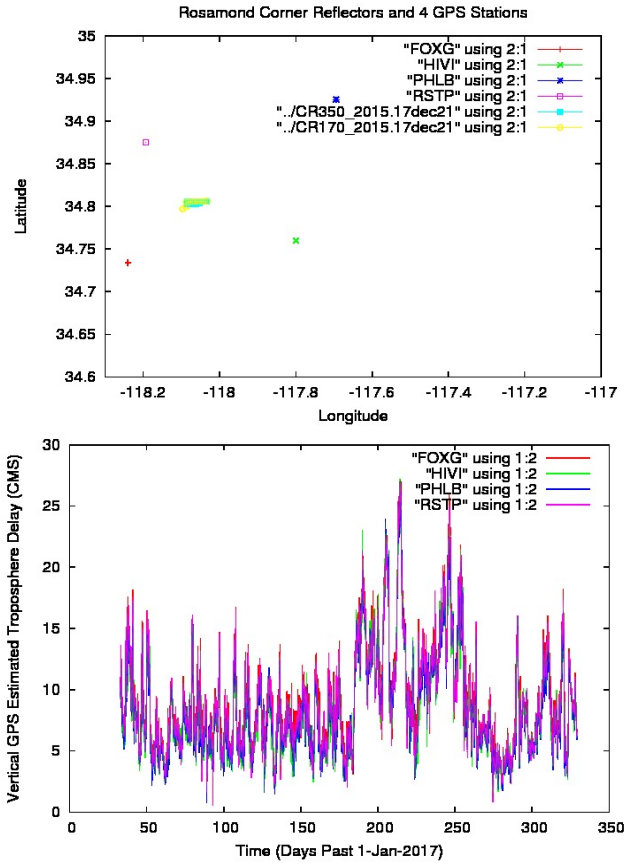

Figure 4. Top: Relative locations of the Rosamond Corner Reflector Array (RCRA) and the four GPS sites: Fox Field, Rosamond, Phillips Lab, and HIVI. Bottom: the troposphere variation of four GPS monuments that straddle the RCRA.

and started attributing this to a radiometric atmospheric delay. This has highlighted that the standard Neill model which is now built into the SAR processor is deemed overly complicated and the problem of routine generation of troposphere solutions for the radar swaths is lacking. Mitigating the troposphere and adjusting the platform baseline due to plate movement should both be addressed to improve future UAVSAR solution.

Comparison of GPS measurements and UAVSAR repeat pass interferometric product shows good near-field agreement between the two, but up to 5 cm of different farther field (Figure 5). We analyzed a product spanning the 2010 M7.2 El Mayor – Cucapah earthquake in which 60 cm of line of sight motion occurred from north to south across the largest displacement in the interferogram [5,14]. GPS stations close to the center of the interferogram, show good agreement with the interferogram, while GPS stations further from the center show worse agreement. Adjusting the interferogram with GPS motions computed for the same time frame is one way to reduce this disagreement. Better knowledge of the troposphere is another way to minimize error in the UAVSAR products.

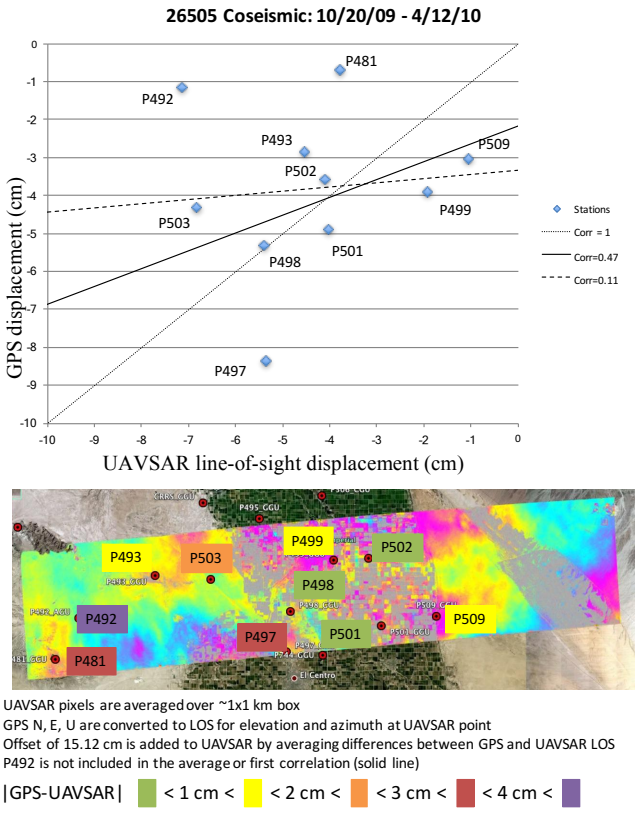

Figure 5. Correlation between UAVSAR and GPS measurements at stations spanning the 2010 El Mayor – Cucapah earthquake. The troposphere is the likely dominant error source.

4. Water Vapor Retrieval/Radiometry

Water vapor in the atmosphere between the land surface and the radar adds a radio path delay of order several to tens of centimeters which distort radar surface topology measurements. To correct these errors, a new millimeter-wave measurement technique has been proposed and tested at JPL which addresses a long-standing problem of how to measure atmospheric water vapor below an aircraft or spacecraft over land surfaces. Radiometers operating near the water vapor absorption lines of 22 GHz and 183 GHz have for many years provided such measurements over open water over oceans. Yet traditional measurement techniques, based on radiative transfer models of the atmosphere, have depended on the predictable reflectivity of the ocean surface in the radio spectrum. Over land, the highly variable scattering and emission from the land surface obfuscate such retrievals.

To solve the overland water vapor retrieval problem, we have developed and demonstrated a new approach which estimates water vapor by comparing spatial contrasts within radiometric images which are attenuated by both oxygen and water vapor. By matching images which are attenuated by water vapor in the 150 to 180 GHz range with images comparably attenuated by oxygen in the 118 to 123 GHz frequency range, data show that it is possible to deduce the unknown amount of water vapor using the known amount of

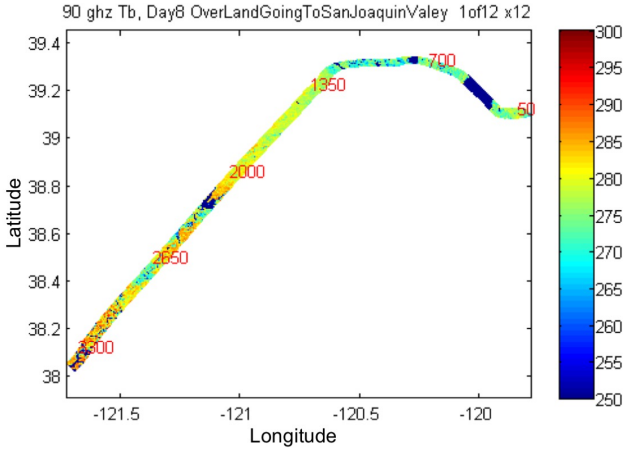

Figure 6. Surface emission map at 90 GHz measured by the HAMMR instrument during a flight between Carson City, Nevada in the northeast, to the San Juaquin Valley of California to the southwest. Scales are of degrees latitude, longitude, and of brightness temperature in Kelvin.

oxygen in the atmosphere. This approach has the advantage of being insensitive to uncertainties of the surface scattering and emission which otherwise render traditional retrievals ambiguous—especially in the lower troposphere where most of the water vapor resides. The new measurement technique is explained using an example data set collected over California in 2014.

Figures 6 and 7 summarize microwave and millimeter-wave radiometric images collected by a NASA airborne radiometer (HAMMR = High altitude Microwave and Millimeter-wave Radiometer) on November 14, 2014 during a flight from Carson City Nevada over the Sierra Mountains and into the San Joaquin Valley of California. The downward viewing, cross-track scan of HAMMR produces imagery of the land surface below the aircraft. These figures show, for example, the large water body of Lake Tahoe between time tags of 50 and 700 seconds, followed by numerous smaller open water features along the Sacramento River in the San Juaquin Valley from 2000 seconds onward. Lesser contrasts occur away from these water bodies—e.g. within between warm fields and cooler forests between 1350 and 2000 seconds. Figure 6 shows the 90 GHz imagery of the land under the aircraft track in a map of true latitude and longitude, whereas Figure 7 summarizes all 18 observing bands of HAMMR for the same segment as plotted in a strip-chart manner. Note that the HAMMR instrument includes fifteen-millimeter bands as well as three microwave bands near 22 GHz. These microwave channels are used below to provide validation of water vapor estimates using traditional radiative transfer techniques wherever open water bodies permit.

In Figure 7 two example time segments have been highlighted around the 120.7 GHz imagery to show matches with corresponding imagery in the 168 to 176 GHz range. In these examples, we see that the 120.7 GHz image matches images at about 176 GHz, initially, and then later 168 GHz.

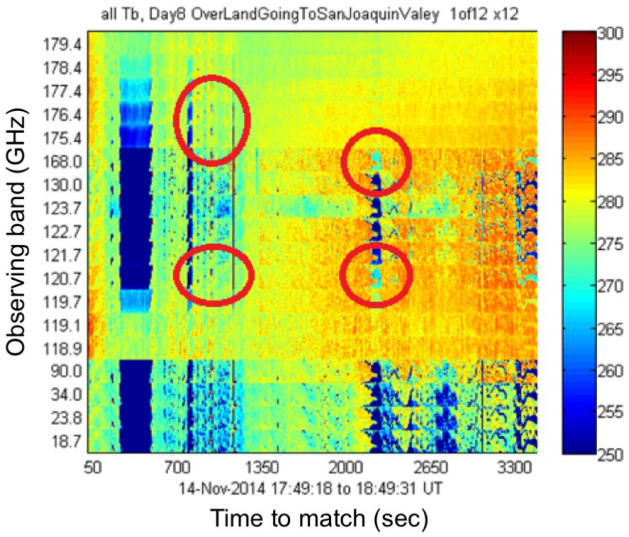

Figure 7. All channels of the HAMMR instrument for same segment of Figure 6. Left scale is observing band in GHz; horizontal scale is of seconds in time to match Figure 6; and color scale is brightness temperature in Kelvin. Each observing band has been plotted for a range of +/- 40 degrees of cross-track scan about the nadir angle. Highlighted regions illustrate examples where image contrasts are matched among the 120.7 GHz channel and various channels from 168 to 177 GHz, depending on water vapor.

This shift of frequency is an indication that water vapor has increased between these two segments.

Atmospheric attenuation models are used to produce quantitative estimate of water vapor from the above observations. Figure 8 illustrates two atmospheric opacity spectra models for the two cases relevant to Figure 7. Markers along the spectra of Figure 8 correspond to the available observation frequencies of HAMMR, and the two horizontal arrows illustrate how the 120.7 GHz opacities are matched with either 176 GHz or 168 GHz, depending on the amount of water vapor in the atmosphere. These correspond to solutions of 3 cm radio path delay due to water vapor (dry case= blue) and 10 cm radio path delay (wet case= green). Similar pairings can be made among the other HAMMR observing bands as well.

Numerically, such path delay estimates are computed for each of 7 available observing bands near the oxygen line from 118.9 to 123.7 GHz. Candidate water vapor levels are tested by computing opacity in a forward model and locating a match between the given oxygen band and an interpolated water vapor band. A "match" is determined by spatially cross-correlating the difference between oxygen and water attenuated image pairs with the clear-sky image at 90 GHz according to

$$R_{ij} = R(f_i, PD_j) \equiv \frac{cov(T_{ij}-T_i, T_{90})}{\sqrt{var(T_{ij}-T_i)var(T_{90})}}. \quad (1)$$

Here, T_i is for example the 120.7 GHz image circled in Figure 7, T_{ij} is a linear interpolation of candidate images (the

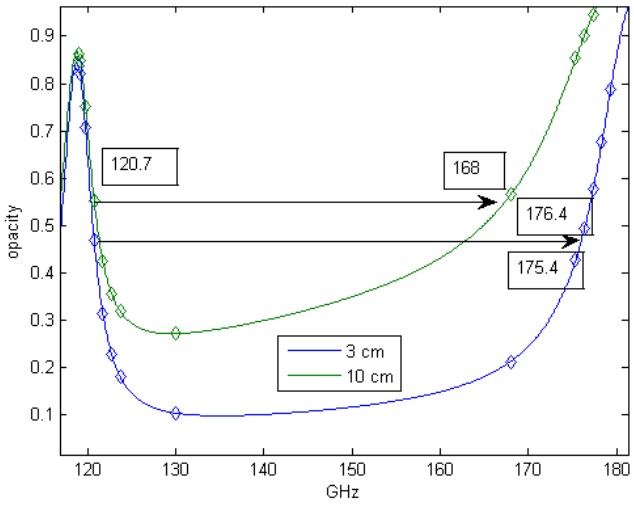

Figure 8. Atmospheric opacity spectra for two cases of 3 cm and 10 cm radio path delay. Opacities near the oxygen line at 120.7 GHz can be reliably modeled and paired with equivalent opacities dominated by water vapor between 150 and 180 GHz.

175.4 and 176.4 GHz images in Figure 7 for a candidate path delay, PD_j, and T_{90} is the 90 GHz image. Interpolations of water vapor sensitive images are formed using the model opacities according to

$$T_{ij} = \frac{o_{jk+1}-o_{ji}}{o_{jk+1}-o_{jk}} T_k + \frac{o_{ji}-o_{jk}}{o_{jk+1}-o_{jk}} T_{k+1}. \quad (2)$$

where T_k and T_{k+1} are for example the 175.4 and 176.4 GHz images in Figure 7, and the opacities, o, are calculated with a model for the test case water vapor, PD_j, as in Figure 8, for two observed water channels, k and k+1, and the interpolated channel.

A zero-crossing in (1) versus water vapor establishes a path delay solution for each of the seven oxygen bands. These seven solutions are then evaluated for consistency and sensitivity to form the final path delay estimate. Figure 9 illustrates the full set of seven solutions formed from the imagery of Figure 7, along with a weighted mean of the seven solutions, and a solution—in effect ground truth—formed using the traditional microwave retrievals over open water (top band). Here, we see remarkably good agreement—both among the seven oxygen bands and with the microwave retrievals where they exist.

The bottom band of Figure 9 also plots a "confidence" parameter. This parameter is a measure of the signal-to-noise, in effect, which is calculated from the derivative of (1) with respect to path delay (PD). Low confidence implies that the covariance calculation in (1) is weak for a wide range of PD, and that the solution may be ambiguous. When this confidence is poor, and the agreement among the seven bands of Figure 9 is also poor, there is good reason to reject the path delay measurement. Conversely, when agreement among the bands, or a low RMS error among the seven PD solutions, is good, and the confidence metric is high, the data can be considered reliable.

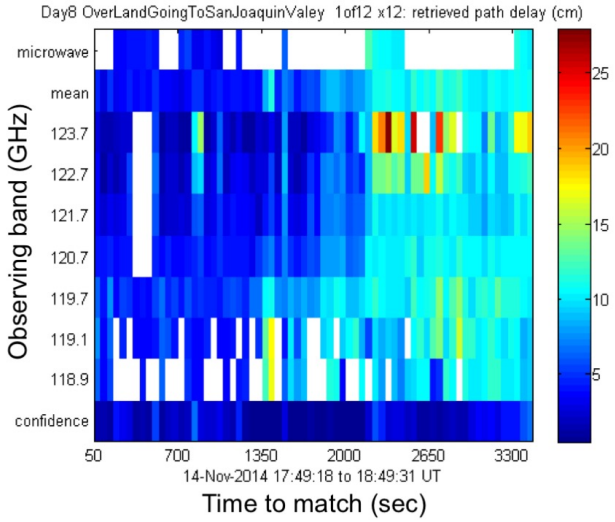

Figure 9. Color-coded breakdown of path delay (color scale in cm radio path delay) as measured by various methods and as measured among all of the available oxygen bands (GHz on left margin) using the technique described in the text.

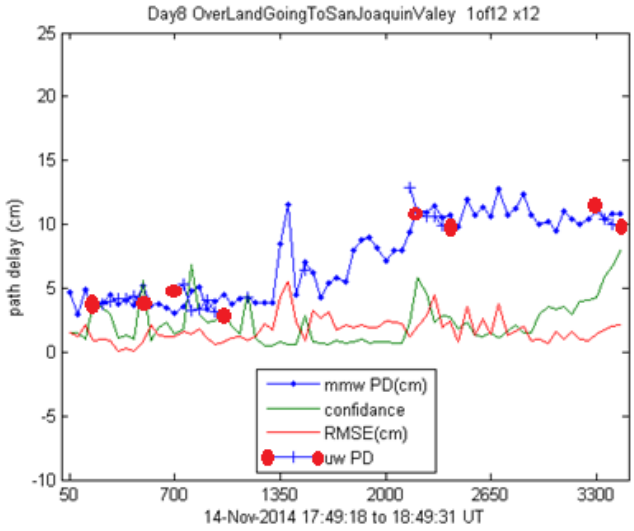

Figure 10. Summary from Figure 9 of the millimeter-wave retrievals of the new approach (mmw PD), the microwave (uw), and the two quality metrics of RMSE and 'confidence' as described in the text.

Using the above concepts, Figure 10 presents a summary of path delay measurement mean and microwave PD from Figure 9, along with the RMS error and confidence metrics. These data show excellent agreement between the traditional microwave radiative transfer solutions over water, and a consistent and reasonably smooth estimate of path delay over dry land between those regions, such as between 1350 seconds and 2000 seconds. There are just a few anomalous points, yet we also note that these anomalies are associated with a high RMS error and a low confidence, and would therefore be easily excised.

3. Topographic Imaging

Including topography from Structure from Motion (SfM) using multiple images improves geodetic imaging observations of earthquake faults. High resolution terrain map (HRTM) measurements can be used to improve baseline estimation of the UAVSAR measurements; currently UAVSAR uses SRTM 30 m postings in their data processing stream. HRTM measurements also provide geomorphic metrics of fault zones, important for comparing current deformation to paleoearthquake history. In disrupted areas where UAVSAR decorrelates, differencing of repeat structure from motion measurements can fill in the gap of missing data, showing images of surface disruption and providing surface change using point cloud differencing. Offset features in single images can also be used to estimate fault slip and surface disruption can be estimated from single images.

Another strength of topographic measurements is the ability to compute 3D motions. InSAR provides line of sight measurements between the instrument and the ground at an oblique angle. Without multiple products of the same area from different vantage points the amount of horizontal and vertical motions and the direction of slip must be estimated using assumptions. 3D motions from GPS provide a rough constraint and geologic field mapping also provides constraints. Topographic change maps would provide 3D changes on a pixel by pixel basis.

UAVSAR observations from the 2014 M6 South Napa earthquake [11,12] show that the UAVSAR observations decorrelated over a 4 km wide zone for about 12 km or along nearly the entire length of the rupture (Figure 11). The rupture along the fault reached up to about 80 cm. The data decorrelated for line-of-sight offsets about 20 cm. One reason for the decorrelation is extensive disruption of the surface where shaking was greatest within 2 km on either side of the rupture.

We have been studying a concept for collecting near-concurrent imagery with UAVSAR with an array of cameras mounted in a nadir port on the UAVSAR aircraft to provide multi-angle imagery from which topography can be determined. The name for the concept is QUAKES, Quantifying Uncertainty and Kinematics of Earth Processes.

To satisfy the science community QUAKES should collects imagery suitable to produce a 12 km cross track, HRTM with 1 m GSD, 1 m altitude error when collecting data on UAVSAR platform operating during a clear day at normal altitude and speed (40K feet—12.5km, 400 knts). HRTM is to be available 1 week after flight. A mosaic image of the 12 km cross track over the path of the UAVSAR is available directly after flight is completed. Images produced are color and the final HTRM is a geo rectified GeoTIFF image.

The derived requirements then are <1 m GSD for a pixel on the ground with > 12000 pixels per cross track line. Images should be color. There is some advantage to infrared bands for penetration smoke or thin clouds, so this is being

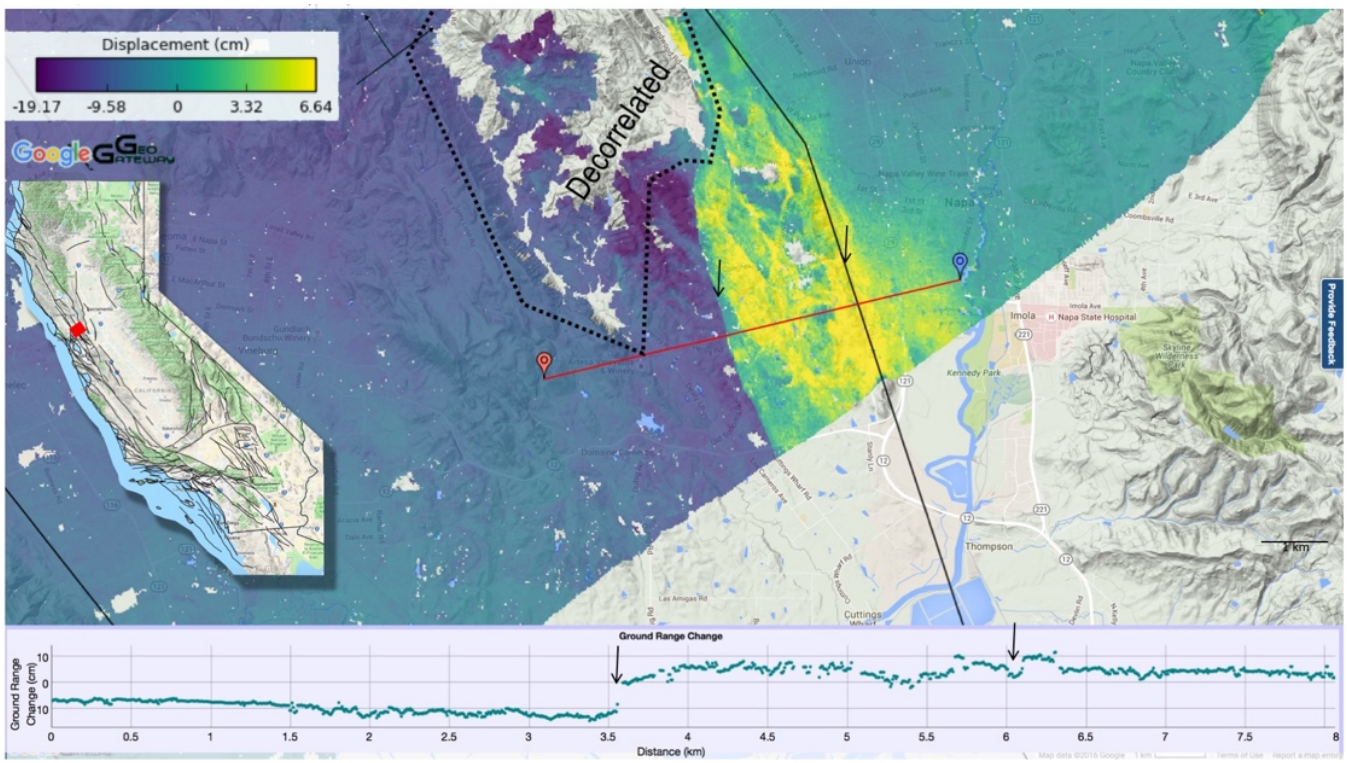

Figure 11. UAVSAR product for the 2014 M6.0 South Napa earthquake with decorrelated area outline in black dotted line and noted.

explored. The image must be in focus for localization to determine spatial features on the order of 1 pixel.

The derived requirements require a camera system with full frame imagers. A > 100 mm lens, integration time for measurement of < 0.5 pixels on the ground, with a flight speed of 200 meters/sec * It < 0.6 meter/pixel * 0.5 pixels requires an integration time < 1.5 msec. Disparity of 0.3 pixels is expected. Image overlap requires minimum of 1 image with ¾ overlap leading to a requirement of > ½ Hertz image sample. Our target is 2 Hz. On Board Electronics must support at least 8 cameras operating at 2 Hz amd support synchronized image acquisition. Data storage is for 6 hours * 3600 sec/hour * 2 /sec * 8 images * 20 MP/image resulting in 7 Tbytes of data per day. 4-8 storage disks disks are required to support writing 8 x 40 mbytes/sec to. 8 cameras would have the following characteristics each: lens focal lengths of 100mm and 135mm, < F/12 , CMV20000 FPA, which is the Mars 2020 EECAM Baseline, and each Bayer coated CMOS visible focal plane. Four cameras would point forward and four aft.

A proof of concept system would have a pair of cameras in a fixed pose. The angular separation of the cameras should be 22.6 degrees, +/-11.3° from nadir. This would provide a synthetic baseline of 5km from a standoff of 12.5km. A crosstrack field of view would be needed to cover 12km on the ground perpendicular to the flight path. As an initial proof of concept, we flew one camera pointed out the window of the Gulfstream-III during a UAVSAR flight (Figure 12). The results are promising. 23 images were collected in a line along the flight path and were processed using the commercial Pix4D software package. Average ground sample distance was 3 m with better results in the near field. The Garlock fault is apparent as are other natural and built features such as trees, buildings, and storage tanks.

Because UAVSAR is side looking, the two instruments will not observe at the same place at exactly the same time, but if a lawnmowing approach is used, the UAVSAR imaged region can be imaged with the framing cameras within about ½ hours. A side looking context camera could image the same area as the UAVSAR radar with lower resolution. Processing of the data will be compute intensive and will need to be processed on the cloud or on a supercomputer such as Pleiades at NASA Ames Research Center. Another way to limit the data processing is to collect baseline imagery for all regions flown with UAVSAR and then target areas where changes are expected.

7. SUMMARY

UAVSAR is a useful platform for measuring surface motions of the Earth's crust in order to understand earthquake fault processes. Using GPS displacement measurements would improve the UAVSAR results and enable measurement of tectonic deformation across the entire swath. This is important because long swaths often cross multiple faults. Mitigation of tropospheric errors would improve the accuracy and thus utility of UAVSAR. Topographic measurements would provide complementary observations that fill in decorrelated gaps in UAVSAR measurements, provide a geomorphic perspective of past earthquakes, and

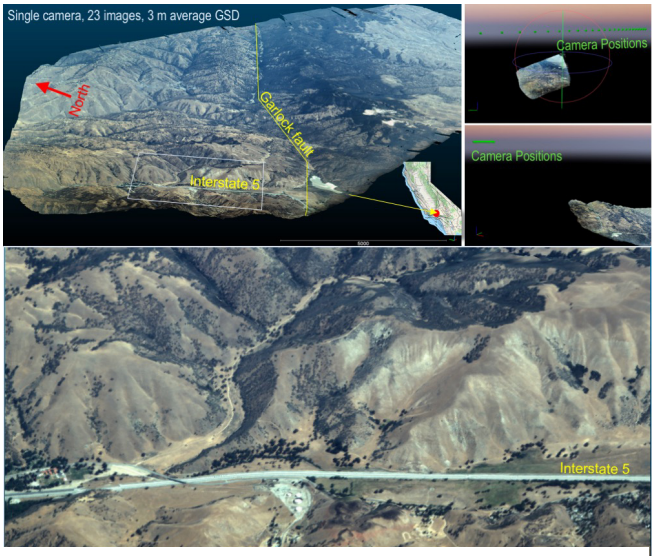

Figure 12. Sample reconstruction collected from a camera pointed out the window at about 45° off nadir during a UAVSAR flight. 23 images from 12.5 km altitude flown in a line were used for the reconstruction. Full image in the top left covers about 20 km from top to bottom of the image. Lower image is about 5 km top to bottom.

maps of 3D change and disturbance between pairs of observations. High resolution topographic measurements would also improve UAVSAR results over current processing methods.

ACKNOWLEDGEMENTS

This work was carried out at the Jet Propulsion Laboratory, California Institute of Technology under contract with NASA. We thank NASA Armstrong Flight Research Center for acquisition of the UAVSAR data and for certifying the vehicle and personnel for carrying out the small UAS flights. Members of the robotics section at JPL for developed the design and carried out the test flights of the camera system. We thank many colleagues for useful science input, including but not limited to Yehuda Ben-Zion from USC, Steve DeLong from the USGS, Ramón Arrowsmith from ASU, Lisa Grant Ludwig from UC Irvine, and John Rundle from UC Davis. Marlon Pierce and Jun Wang from Indiana University support GeoGateway which was used for access to and analysis of UAVSAR and GPS data products.

REFERENCES

[1] Petersen, M. D., Moschetti, P. M., Powers, P. M., Mueller, C. S., Haller, K. M., Frankel, A. D., Zeng, Y., Rezaeiam, S., Harmsen, S. C., and Boyd, S., et al., 2014. Documentation for the 2014 update of the United States national seismic hazard maps, U.S. Geol. Surv. Open-File Rept. 2014-1091, 243 pp.

[2]Rosen, P.A., Hensley, S., Wheeler, K., Sadowy, G., Miller, T., Shaffer, S., Muellerschoen, R., Jones, C., Zebker, H. and Madsen, S., 2006, April. UAVSAR: A new NASA airborne SAR system for science and technology research. In Radar, 2006 IEEE Conference on (pp. 8-pp). IEEE.

[3] Delbridge, B.G., Bürgmann, R., Fielding, E., Hensley, S. and Schulz, W.H., 2016. Three-dimensional surface deformation derived from airborne interferometric UAVSAR: Application to the Slumgullion Landslide. Journal of Geophysical Research: Solid Earth, 121(5), pp.3951-3977.

[4] Jones, C., Bawden, G., Deverel, S., Dudas, J. and Hensley, S., 2011, July. Characterizing land surface change and levee stability in the Sacramento-San Joaquin Delta using UAVSAR radar imagery. In Geoscience and Remote Sensing Symposium (IGARSS), 2011 IEEE International (pp. 1638-1641). IEEE.

[5] Donnellan, A., Parker, J., Hensley, S., Pierce, M., Wang, J. and Rundle, J., 2014. UAVSAR observations of triggered slip on the Imperial, Superstition Hills, and East Elmore Ranch Faults associated with the 2010 M 7.2 El Mayor-Cucapah earthquake. Geochemistry, Geophysics, Geosystems, 15(3), pp.815-829.

[6] Donnellan, A., Grant Ludwig, L., Parker, J.W., Rundle, J.B., Wang, J., Pierce, M., Blewitt, G. and Hensley, S., 2015. Potential for a large earthquake near Los Angeles inferred from the 2014 La Habra earthquake. Earth and Space Science, 2(9), pp.378-385.

[7] DeLong, S.B., Donnellan, A., Ponti, D.J., Rubin, R.S., Lienkaemper, J.J., Prentice, C.S., Dawson, T.E., Seitz, G., Schwartz, D.P., Hudnut, K.W. and Rosa, C., 2016. Tearing the terroir: Details and implications of surface rupture and deformation from the 24 August 2014 M6. 0 South Napa earthquake, California. Earth and Space Science, 3(10), pp.416-430.

[8] Zumberge, J.F., Heflin, M.B., Jefferson, D.C., Watkins, M.M. and Webb, F.H., 1997. Precise point positioning for the efficient and robust analysis of GPS data from large networks. Journal of Geophysical Research: Solid Earth, 102(B3), pp.5005-5017.

[9] Chen, Curtis W., and Howard A. Zebker. Network approaches to two-dimensional phase unwrapping: intractability and two new algorithms. J. Opt. Soc. Am. A, 17(3):401{414, Mar 2000.

[10] Goldstein, Richard M., Howard A. Zebker, and Charles L. Werner. Satellite radar interferometry: Two-dimensional phase unwrapping. Radio Science, 23(4):713{720, Jul 1988.

[11] Hensley, S., T. Michel, M. Simard, C. Jones, R. Muellerschoen, C. Le, H. Zebker, and B. Chapman. Residual motion estimation for UAVSAR: Implications of an electronically scanned array. In 2009 IEEE Radar Conference, pages 1{5, May 2009.

[12] Atwater, T. and Stock, J., 1998. Pacific-North America plate tectonics of the Neogene southwestern United States: an update. International Geology Review, 40(5), pp.375-402.

[13] Rymer, M.J., Treiman, J.A., Kendrick, K.J., Lienkaemper, J.J., Weldon, R.J., Bilham, R., Wei, M., Fielding, E.J., Hernandez, J.L., Olson, B.P. and Irvine, P.J., 2011. Triggered surface slips in southern California associated with the 2010 El Mayor-Cucapah, Baja California, Mexico, earthquake (No. 2010-1333). US Geological Survey.

[14] Donnellan, A., Parker, J., Heflin, M., Lyzenga, G., Moore, A., Ludwig, L.G., Rundle, J., Wang, J. and Pierce, M., 2018. Fracture Advancing Step Tectonics Observed in the Yuha Desert and Ocotillo, CA, Following the 2010 Mw7. 2 El Mayor-Cucapah Earthquake. Earth and Space Science.

BIOGRAPHIES

Andrea Donnellan *is a principal research scientist at NASA's Jet Propulsion Laboratory. She is an editor of the American Geophysical Union journal Earth and Space Science. In 2018 she was a lecturer at California State Polytechnic University, Pomona and past President of the American Geophysical Union's Nonlinear Geophysics Focus Area. Donnellan received a B.S. in geology from the Ohio State University in 1986, an M.S. and Ph.D. in geophysics from Caltech in 1988 and 1991 respectively, and an M.S. in Computer Science from the University of Southern California in 2003. She was Principal Investigator of QuakeSim, now called GeoGateway, which won NASA's 2012 Software of the Year Award. Donnellan has been Deputy Manager of the JPL's Science Division, Pre-Project Scientist of what is now the NISAR radar mission, and NASA's Applied Sciences Program Area Co-Lead for Natural Disasters.*

Curtis Padgett *is a Principal Robotics Technologist and Group Supervisor at the Jet Propulsion Laboratory. He has over 20 years of experience developing perception and sensing systems for autonomy applications for water, aerial, and space for NASA, ONR, AFRL, DARPA and commercial companies. His expertise is in computer vision, pattern recognition/classification, vision-based mapping and geolocation, and imaging sensor systems. He received his Ph.D. in Computer Science at the University of California, San Diego in 1997.*

Yunling Lou *received the B.S. and M.S.E. degrees from University of Texas, Austin and University of Pennsylvania respectively. She is currently Supervisor of the Suborbital Radar Science and Engineering Group at the Jet Propulsion Laboratory, California Institute of Technology in Pasadena, California, where she manages UAVSAR project, NASA's airborne imaging radar test-bed for future imaging radar missions. Besides instrument operation and delivering calibrated UAVSAR data products, her group develops new SAR imaging techniques and signal processing algorithms, including repeat-pass interferometry to measure crustal deformation and land subsidence, and polarimetric interferometry and tomography to study forest structure. Her group is also developing near real-time onboard processing capabilities for rapid response of hazards.*

Dr Alan B Tanner *is a principal engineer at NASA's Jet Propulsion Laboratory, where he has been employed since 1989. He specializes in the design and calibration of microwave radiometers and scatterometers for remote sensing of the earth. Alan has been the lead system engineer for the Geostationary Synthetic Thinned Array Radiometer (GeoSTAR), the Ultra-Stable Radiometer testbed (which formed the basis of the Aquarius and Juno radiometer designs), the Advanced Water Vapor Radiometers (AWVR) for the Cassini Gravitational Wave Experiment, the Airborne Cloud Radar (a 94 GHz scatterometer which preceded the CloudSat mission), and the Airborne Rain Mapping Radar (for Tropical Rainfall Measurement Mission). For his graduate work at the University of Massachusetts Microwave Remote Sensing Lab (MIRSL), he developed the Electronically Scanned Thinned Array Radiometer (ESTAR) for soil moisture measurements, and the Stepped Frequency Microwave Radiometer (SFMR) for hurricane wind speed detection.*

Jay Parker *is a Senior Scientist in the Geodynamics and Space Geodesy group at NASA's Jet Propulsion Laboratory. He is co-investigator of GeoGateway, which supplies a variety of crustal deformation information in a public map-based web interface. With the QuakeSim team he received NASA's Software of the Year Award, in 2012. He develops algorithms for surface fracture measurements in radar image pairs, and implements modeling and analysis applications for a variety of Earth remote sensing applications. These include finite element simulations of crustal deformation due to fault motions, ocean sensing through GPS signal reflection, scalable algorithms for electromagnetic scattering and radiation, and line-by-line simulation and retrieval of atmospheric parameters from high resolution infrared sensors. His graduate work at University of Illinois analyzed and modeled features found in mesospheric observations, including solar flare response and the transition to turbulence. His PhD is from UIUC, 1988, and BS from the California Institute of Technology in 1981 (all Electrical Engineering).*

Brian Hawkins *received the B.Sc. and M.Sc. degrees in aerospace engineering from the University of Texas at Austin in 2006 and 2009. He joined the staff of the Jet Propulsion Laboratory, California Institute of Technology, Pasadena, in 2009 where he has worked on various airborne and spaceborne synthetic aperture radar projects. His interests include radar processing algorithms, calibration, and applications as well as embedded, real time processing systems.*

Adnan Ansar *supervises the Aerial and Orbital Image Analysis group in the Robotics Section at NASA's Jet Propulsion Laboratory. He is an expert in geometric computer vision and has worked extensively under multiple NASA and reimbursable efforts in camera calibration, image-based pose estimation, structure from motion and 3D scene reconstruction. He is the author of the survey-free calibration technique used throughout the Robotic Section, has developed prototype 3D reconstruction techniques for the AFRL Angelfire program, demonstrated cross-modal image registration methods for Titan balloon localization under NASA ROSES funding, and has developed Mars surface model reconstruction capabilities for the MRO HiRISE and CTX imagers. He received a BA (1993) in Physics, MA (1993) in Mathematics, MS (1998) in Computer Science and PhD (2001) in Computer Science all from the University of Pennsylvania, with the last earned at the GRASP Laboratory.*

Michael Heflin *earned a PhD in Physics from MIT and has worked for over twenty five years at the Jet Propulsion Laboratory. Research topics include gravitational lensing, aperture synthesis imaging, optical interferometry, celestial and terrestrial reference frames, GNSS data processing, and modeling of crustal deformation signals. He has won JPL's Award for Excellence, appeared on NBC Nightly News, and been inducted into to the Space Technology Hall of Fame. He is co-author of JPL's GipsyX software and has automated weekly GNSS time series updates available at: https://sideshow.jpl.nasa.gov/post/series.html*

Joseph J. Green *is a principal optical engineer at NASA's Jet Propulsion Laboratory. For the past 19 years he has advanced the state of the art in wavefront sensing and control, optical system modeling, high-contrast imaging and image processing on many projects including JWST, TPF, SIM, Spitzer and Mars 2020. He received his Ph.D. in Electrical Engineering from the University of Arizona in 2000. In 2007 he was part of the JPL team that won the NASA Software of the Year Award for their MGS wavefront sensing software.*

Ron Muellerschoen *joined Jet Propulsion Laboratory as a member of the technical staff in 1985 in the Navigation Systems Section. He worked in the Earth Orbiter Systems Group in 1992 where he developed NASA's Global Differential Global Positioning System. He is one of the primary authors of GIPSY/OASIS, Real-Time GIPSY (RTG), and Real-Time Net Transfer (RTNT). He is currently a senior member of technical staff in Suborbital Radar Science and Engineering group of the Radar Science and Engineering Section.*